

Ground and flight performance of the balloon-borne magnetic spectrometer AESOP-Lite

The AESOP-Lite collaboration

^a*Santa Cruz Institute for Particle Physics, Physics Department, University of California Santa Cruz, Santa Cruz, CA 95064*

^b*Bartol Research Institute, University of Delaware, Newark, DE 19716*

Abstract

The Anti-Electron Sub-Orbital Payload Low Energy (AESOP-Lite) is designed to explore the origin of the negative spectral index in the cosmic ray electron spectrum below 100 MeV through a series of balloon flights. The original entry telescope from the Classic LEE (Low Electron Energy) instrument has been directly integrated in AESOP-Lite. The instrument utilizes a gas Cherenkov and magnetic spectrometer configuration to identify particle type and determine the energy. The first flight took place May 15-21, 2018 from Kiruna, Sweden accumulating roughly 130 hours of exposure above 130,000 feet altitude before landing on Ellesmere Island, Canada. In this paper, we report on its design, calibration and performances. This includes the analyses of ground data taken during the integration of the detector before the flight. The observed muon charge separation from ground runs is discussed and compared to the expected performance of the spectrometer. The energy resolution from track reconstruction algorithms and the energy-dependent geometry factor are tested with Monte Carlo simulations. Finally, we present a brief overview of the 2018 flight and preliminary results of the detector performances in flight.

Keywords: cosmic rays - solar modulation - magnet spectrometer - balloon instrumentation

1. Introduction

The past decade has witnessed a new dawn in precision measurements of cosmic rays, with the launch of space-borne instruments such as PAMELA [1] and AMS-02 [2], as well as the more recent CALET, DAMPE, and ISS-CREAM experiments [3, 4, 5]. However, none of them has the sensitivity to study the lower range of the electron spectrum. Below 100 MeV, the effects of solar modulation at 1 AU can now be directly compared to the unmodulated VLIS (Very Local Interstellar Spectrum) probed by the Voyager spacecrafts [6]. For this purpose, we have designed, built, and flown a balloon-borne magnet spectrometer to measure electron and positron cosmic rays from 20 MeV to 300 MeV. AESOP-Lite successfully completed its first mission in May 2018, on a 5-day flight between Esrange, Sweden (66°89'N) and Ellesmere Island, Canada (78°40'N), on a NASA 40 million cubic foot, zero pressure, long duration balloon.

The AESOP-Lite instrument inherits its entry telescope from the well-traveled LEE (Low Electron Energy) payload [7]. Developed in the late 1960's at the University of Chicago, LEE provided pioneering measurements of low energy electrons [8] over the course of 23 flights, the last of which occurred in 2011. LEE's observations have highlighted the mysterious turn-up in the electron spectrum around 80 MeV and the discrepancies between observations in the inner and outer heliosphere (see Fig. 3 in ref.[9]). No further conclusions can be reached until si-

multaneous measurements of electrons and positrons are made. Noteworthy to mention is the fact that the positron spectrum has never been resolved below 100 MeV, whereas in widely discussed results, PAMELA, Fermi-LAT, AMS-02 reported a positron fraction higher than the one predicted for a purely secondary model at energies above 1 GeV [10, 2, 11]. Thus, it was with the objective of extending measurements made by PAMELA and AMS-02 to the low-energy regime below 300 MeV that the AESOP-Lite mission was designed. As it aspires to the longevity of its predecessor LEE, we wish in this paper to introduce the AESOP-Lite instrument and describe in some detail its detector system and capabilities.

2. The detector system

The first consideration to reckon with in designing the new payload is the reduced weight required to reach higher altitudes on a balloon, in order to minimize the contribution of secondary cosmic rays produced in the residual atmosphere. Eliminating the LEE calorimeter aids that objective. In addition, the geometry factor must be such that good statistical accuracy can be reached, despite the low flux of primary electrons. The new instrument, consisting of an entry telescope and a magnetic spectrometer, roughly retains the acceptance of the LEE instrument.

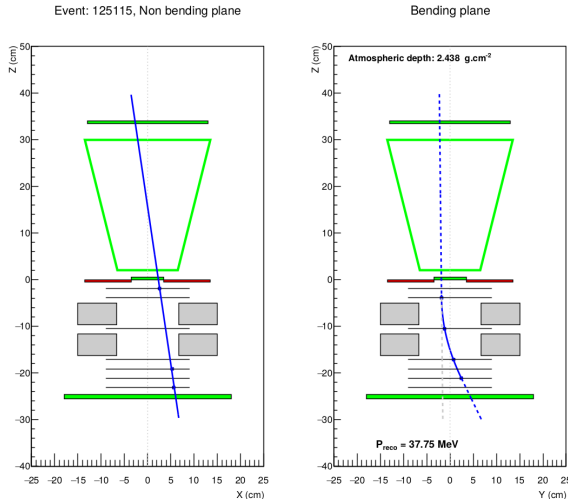


Figure 1: Event display of an electron candidate recorded during the 2018 flight. The triggers T1, T2, T3 and T4 were fired (in green) whereas no signal was seen in the guard (in red).

2.1. Entry telescope

Fig. 1 shows a schematic cross section of the instrument. The entry telescope, taken from LEE, consists of three NE 102 A plastic scintillators (T1, T3 and Guard) and a gas Cerenkov detector (T2). T1 and T3 both aid in identifying singly charged relativistic particles, while T2 serves primarily to reject hadrons (protons make up $\sim 90\%$ of primary cosmic rays [12]). The Cerenkov counter is filled with C_3F_8 gas overpressured at 1.8 atm, to reject all particles with $\gamma = E/mc^2 \leq 15.7$ (corresponding to an electron or positron energy of approximately 8 MeV). Furthermore, it is sensitive only to downward-moving particles, thus rejecting the upward-going splash albedo present in the atmosphere. The combination T1-T2-T3 defines the geometry factor of the instrument ($15\text{cm}^2\text{sr}$), with a maximal acceptance angle of 27.5° from vertical. The coincident signal T1-T2-T3 was used in flight as the main instrument trigger, together with a trigger from the tracking system (a T1-T2-T4 trigger was also used for a short period of time). The guard counter (G), used strictly offline, serves to veto events with particles produced by showers inside the apparatus, while the plastic scintillator T4, placed at the very bottom, detects particles that have completely penetrated the instrument.

The entry telescope, including the pulse-height analysers and front-end electronics of each counter-PMT system, was used in LEE flights, providing a means to cross-calibrate the AESOP-Lite absolute electron fluxes with previous measurements. The similarity with the ancestral LEE instrument ends there however: the novelty of AESOP-Lite lies in the use of a magnetic spectrometer capable of distinguishing positrons from electrons, replacing the calorimeter previously employed, which was insensitive to the charge sign.

2.2. Magnetic spectrometer

The magnetic spectrometer consists of a tracking system composed of seven planes of silicon strip detectors (SSDs) and a Halbach ring dipole magnet [13], which produces a field that points primarily in the $+x$ direction (see Fig. 1). The average B_x in the symmetry plane is 0.33 T. Across the magnet bore, in the symmetry plane, it varies by as much as 3.2%, whereas the variation within the bore along the symmetry axis is 27%. The integral of B_x along the symmetry axis from $z = -20\text{ cm}$ to $z = +20\text{ cm}$ is 0.057 T m.

The detectors are arranged in an xy -configuration, with four layers in the bending plane to measure the particle deflection, and three layers to view the trajectory in the non-bending plane. The split magnet design allows a tracking layer to be easily placed in the bending view at the center of the field, thus optimizing the momentum resolution.

The SSDs were custom designed and manufactured by Hamamatsu Photonics for the Large Area Telescope (LAT) of the NASA Fermi gamma-ray telescope mission [14]. Each sensor is an $8.95 \times 8.95\text{ cm}^2$, $400\text{ }\mu\text{m}$ thick single-sided detector, with a strip width of $56\text{ }\mu\text{m}$ and pitch of $228\text{ }\mu\text{m}$. A bias potential of $\sim 120\text{ V}$ is applied across the n -type bulk material between the strips and the back-side electrode. Each p -type strip implant is AC-coupled to an aluminum strip just above and biased through a $\sim 50\text{ M}\Omega$ polysilicon resistor.

Aluminum strips and bias rings on pairs of sensors are wire bonded together to form ladders. The ladder strips are then wire bonded to aluminum traces on single-layer glass "pitch-adapter" circuits, which in turn are wire bonded to the readout integrated circuits. The positive bias voltage is applied directly to the backs of the sensors through conductive epoxy that attaches them to printed circuits that are cut out under the sensor active areas. Fig. 3 shows a photograph of one of the seven tracker modules.

Each SSD strip is connected to a channel of one of the twelve 64-channel readout ASICs (Application Specific Integrated Circuit) [15], which were designed for the tracking readout of a prototype proton-CT scanner [16]. The chips are capable of more than ten times faster readout than those used in the Fermi LAT, which is not relevant to the low rates of AESOP-Lite, but they are also easier to use and configure for this application. Each channel has a charge-sensitive amplifier followed by a shaping amplifier and discriminator. The shaping time constant has two digitally configured settings and can also be adjusted by external resistors. For AESOP-Lite it is about a microsecond, resulting in an effective noise charge at the input of ~ 1200 electrons and a signal-to-noise ratio for minimum ionizing particles of ~ 27 .

The discriminator thresholds are set by a single internal DAC per chip. The discriminator output goes into a logical OR of all channels to provide an asynchronous trigger output, and it is also sampled by the clock within

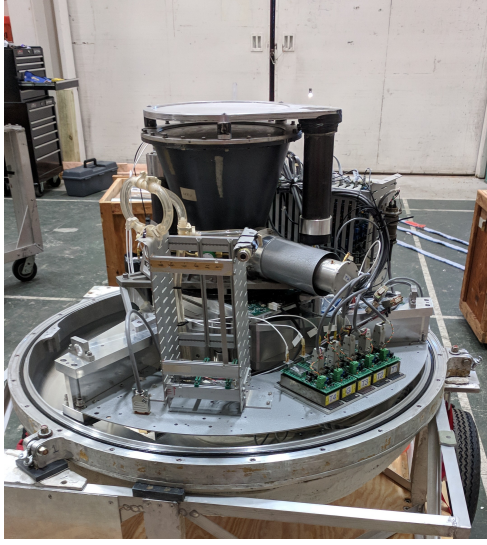


Figure 2: Photograph of the AESOP-Lite instrument with the pressure-vessel “shell” removed.



Figure 3: Photograph of one of the seven tracker modules. The SSD sensor strips are wire-bonded to form two-sensor ladders. The 768 channels are wire bonded to 12 readout ASICs via glass-substrate pitch-adapter circuits.

an adjustable window and buffered pending a trigger decision. Hits above threshold are output by command as a list of strip clusters. Two 64-bit masks can be used to remove individual channels from respectively the trigger output and the data flow.

The cluster lists are buffered for up to four events (although this buffering is not used for AESOP-Lite) and delivered by LVDS (Low-Voltage Differential Signaling) in twelve serial streams to a Xilinx Spartan-6 FPGA operating with the same 10 MHz clock as used by the ASICs. The FPGA firmware configures and monitors the tracker, and the seven FPGAs work together to deliver the data to the FPGA of the top, master board, which then sends the data by a 115200 baud UART to the AESOP-Lite data acquisition.

The FPGAs communicate with each other at 10 million bits per second by LVDS signals transmitted over CAT-5 cables. They also sample the ASIC trigger signals, make a logical OR of the signals from the twelve chips, and pass the results from one bending-plane board to the next and from one non-bending-plane board to the next. The master board thus receives two trigger coincidence signals, one from the bending view and one from the non-bending view. The tracker trigger is an OR of those two signals.

The coincidence signal from the AESOP-Lite scintillators proved to be too slow, with too much jitter, to trigger the tracker reliably, requiring use of the internal tracker trigger for all data acquisition. The tracker holds its data following each tracker trigger until a “go” signal is received by the tracker master board from the T1-T2-T3 coincidence. If five microseconds pass with no “go” signal received, then the tracker data are discarded. There is no buffering of events in the system. Instead the trigger is disabled until the event readout is completed or the data are discarded for lack of a “go” signal, a simple solution allowed by the low cosmic-ray rate.

3. Instrument performance

3.1. Geometry factor

Following the method outlined in [17], we use Monte Carlo simulations to determine the geometry factor of the AESOP-Lite instrument for each particle type studied and each zenith-angle bin. The right panel of Figure 4 shows the acceptance for electrons when imposing the flight trigger requirements: a signal in T1, T2 and T3, and a simulation of the internal tracker trigger. As expected, the geometry factor grows with increasing momentum, as the deflecting effects of the magnetic field are mitigated: the acceptance is $\sim 7 \text{ cm}^2 \text{ sr}$ at 30 MeV/c and $\sim 14 \text{ cm}^2 \text{ sr}$ at 300 MeV/c.

3.2. Track Reconstruction

Once an event has successfully passed the selection criteria of the online trigger coincidence (for instance T1-T2-T3), it is first processed with a pattern recognition (PR)

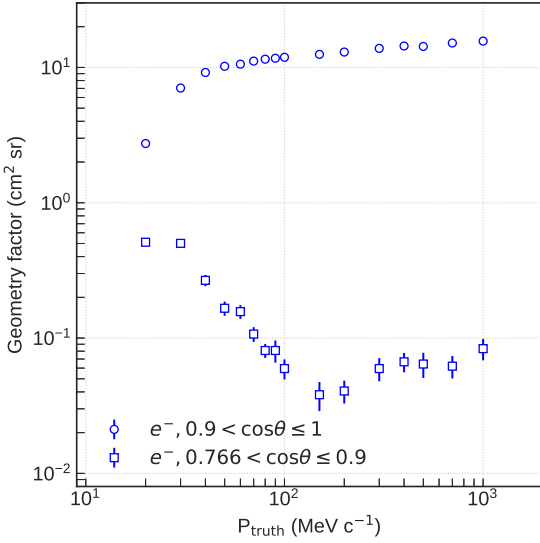


Figure 4: (Left) Model of the AESOP-Lite instrument²⁴⁵ viewed in the graphical interface Flair. (Right) Simulated post-trigger geometry factor for electrons. The calculations are made for two ranges of incident angle θ .

routine that selects hits belonging to a same track: *i*) in the non-bending view, the algorithm fits all possible lines between the top-most and bottom-most layers, and chooses the track that minimizes the χ^2 ; *ii*) similarly in the bending view, a parabola is fit to all possible configurations of hits in the four layers of the plane and the best fit is chosen. From the radius of curvature of the parabola, the momentum of the particle can be inferred. The value from the PR fit is then used to initialize the final reconstruction method. However, for this preliminary analysis, the PR²⁶⁰ routine was used as the primary reconstruction technique. A Kalman Filter [18] and an algorithm that employs simplex minimization of Runge-Kutta integrations have also been developed and are being tested for track fitting. Figure 1 illustrates the parabola fit and straight line fit as seen²⁶⁵ in solid blue lines in our event display tool. The dashed lines in the bending plane panel indicate the incoming and outgoing trajectories of the particles, assuming no scattering or interaction in the detector.

Since the distribution of the reconstructed inverse momentum—and not the momentum itself—follows a normal distribution, we derive for each reconstructed energy and bin in zenith angle, θ , the $1/p_{\text{reco}}$ distribution and fit it to a Gaussian function. The reconstruction p.d.f. also contains the information of the particle’s energy loss, as it will have²⁷⁵ traversed the pressure vessel wall, the scintillators T1 and T3, as well as the C_3F_8 Cherenkov gas prior to reaching the spectrometer. The resolution, bias, and efficiency of the reconstruction are thus parametrized for 16 energies for electrons and positrons. Some examples of p.d.f. are²⁸⁰ shown in the left panel of Fig. 5. The parameters of the fits are then individually and linearly interpolated to extend

the knowledge to the entire energy range of the instrument. The same method is used for all particle types.

On average, we estimate the compounded energy loss to be ~ 4 MeV, a value independent of the energy of the incident particle. The center panel in Figure 5 presents the resolution of our current reconstruction algorithm for electrons: it is about 11.5% at 30 MeV/c and 13.5% at 300 MeV/c. The right panel in Figure 5 shows the efficiencies (post-trigger) of the selection applied to the hits occupancy in the tracker (a number of hits between 5 and 12), and the PR. The distribution shows that the highest efficiency is in our range of interest, i.e., between 30 and 100 MeV/c. Similar results are obtained for positrons.

3.3. Ground runs

Ground runs with different trigger configurations were performed in Esrange prior to the flight. In particular, the simple coincidence of signals in the scintillators T1 and T4 allowed us to accumulate tracks in the spectrometers without vetoing any contributions from muons with insufficient energy to produce Cherenkov light in T2. We applied an anti-coincidence offline veto on T2 to select only the low energetic muons and test our ability to separate and identify positively and negatively charged particles. Figure 6 shows the measured distribution of the signed inverse-momentum. We compare it with simulated distributions that combine a realistic spectrum of Galactic Cosmic Rays at the top of the atmosphere, atmospheric interaction shower [?], and the performances of detection presented previously in this paper. The charge separation is observed with a higher contribution of the positively charged muons as expected, as a majority cosmic rays is positively charged. There is a reasonably good agreement between calculations and observations. The measured double peaks are located at the same signed inverse-momentum as simulated. However they are slightly wider than the expected peaks. This possibly indicates an over-estimation of the calculated reconstruction resolution in the momentum range of several hundreds of MeV/c.

Uncertainties on the simulated muon spectrum at ground level cannot be neglected as a possible explanation. The peak-to-peak atmospheric muon charge ratio μ^+/μ^- is observed at 1.33 ± 0.07 (statistical uncertainty only), a value close to the measurement made by CMS below 100 GeV [19].

If, however, we require offline for T2 to be have been fired, the distribution is then dominated by low-energy electrons and positrons, as well as high-energy muons that appear as quasi-straight tracks (7 mrad deflection at 1.5 GeV). We can determine Maximum Detectable Rigidity (MDR) of the spectrometer by fitting a Gaussian function to the inverse momentum signal (Fig. 7), from which we calculate the $\text{MDR} = 1/3\sigma_{\text{reso}} = 590$ MV. This rigidity range is amply separated from the background of highly relativistic protons encountered during flight. The cosmic ray events collected from ground runs were processed with track re-

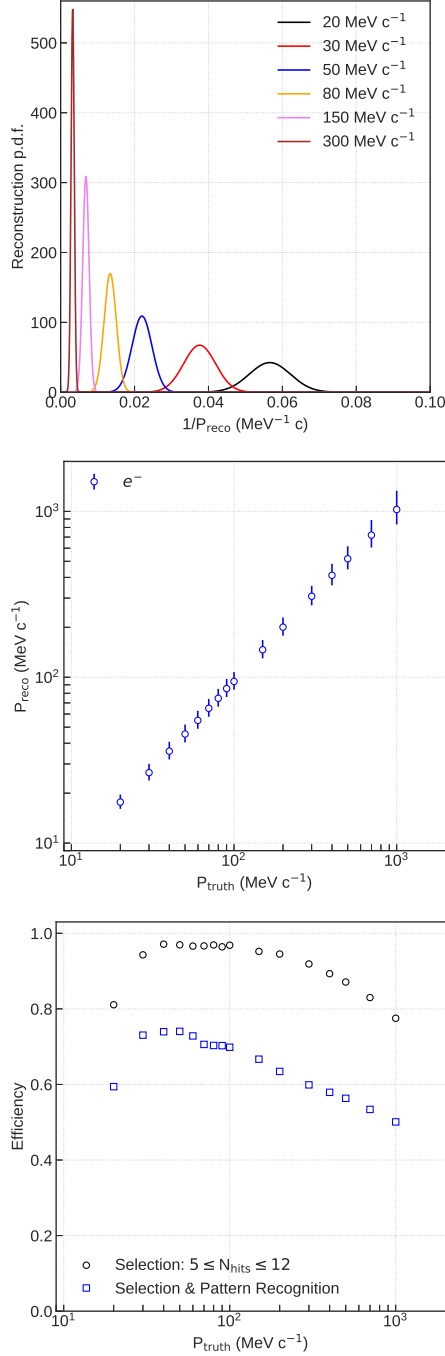


Figure 5: (Left) Reconstruction probability density function for the electrons (incidence: $0.9 < \cos \theta < 1$). (Center) Resolution of the momentum reconstruction for electrons and (right) the associated efficiency.

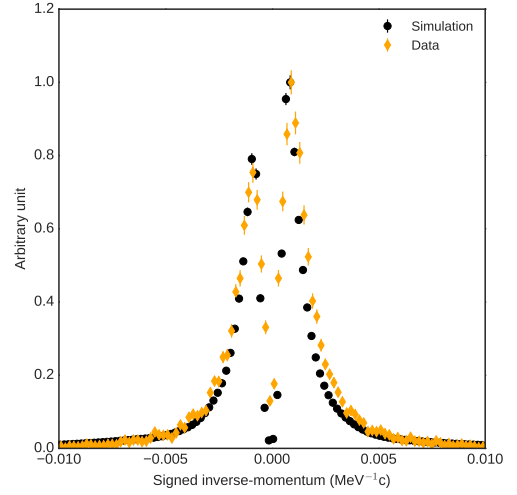


Figure 6: Ground level distribution of the signed inverse-momentum of muons as measured by AESOP-Lite in May 2019 at ESRANGE (orange diamonds) and estimated by simulation (black markers). Histograms are normalized to 1 at their maximum.

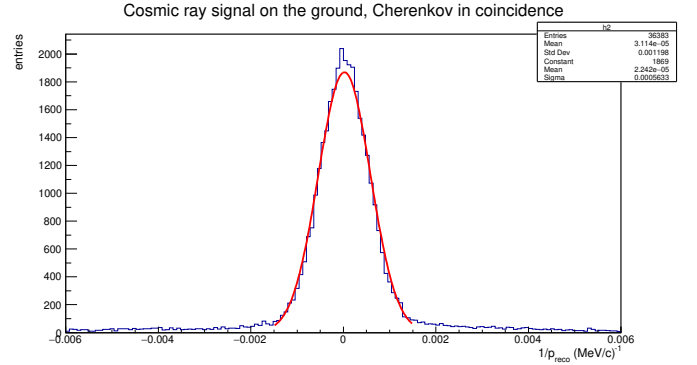


Figure 7: Cosmic ray signal on the ground with T1-T2-T3-T4 requirement

construction algorithms developed with Monte Carlo simulations.

285 4. 2018 campaign and future prospects

AESOP-Lite launched from ESRANGE, Sweden for a 133 hour-long flight at an average altitude of 41 km. It landed on Ellesmere Island, Canada. The northerly trajectory of the payload (see Fig. 7) allowed to survey regions of low (below 0.2 GV) rigidity cutoff (the minimum rigidity a particle must have to enter the magnetosphere at a certain location).

In flight configuration, the instrument was enclosed in an aluminum pressure vessel covered by a polyurethane foam of 2.5 cm thickness. The total weight of the gondola, including the batteries and solar panels, was 390 kg. The payload launched with an additional 270 kg of ballast.

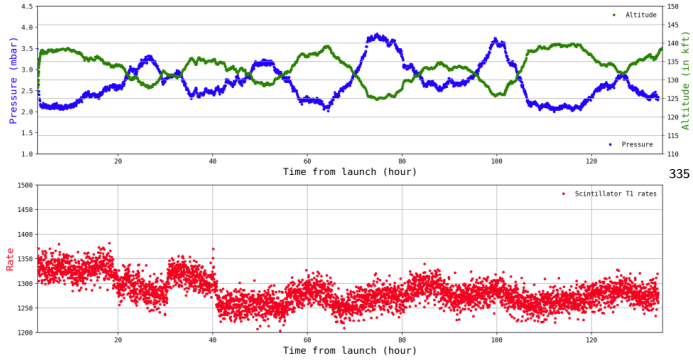


Figure 8: Top panel shows the pressure and altitude flight profile. As the sun sets below the horizon, the volume of the balloon shrinks and its altitude drops, which explains the diurnal variations. Bottom panel illustrates the time profile of T1 scintillator count rate, revealing diurnal variation in the cosmic ray flux

Calibrations of the two barometers of the AESOP-Lite instrument were performed in Palestine, Texas and Es-350 range, Sweden prior to the AESOP-Lite maiden flight. The barometers were used in flight to record the pressure outside the shell, measuring the float altitude and atmospheric overburden. Accurate knowledge of the altitude is neces-355 sary in order to compare flight data with a MC shower model of the cosmic-ray secondary background.

Three self-activating heaters maintained the temperature inside the shell in the neighborhood of 20° C. Four-360 100 Watt solar panels provided power to the instrument in flight, which used 73 W with the heaters on. Three telemetry channels were used for monitoring the good health of the apparatus and receiving data in live time: S-band-365 (frequency range of 2 to 4 GHz), line-of-sight (for a surprisingly long 40 hours), low-rate Iridium (for housekeeping information), and high-rate Pilot Iridium. Each one was doubly redundant, with two operative communication-370 lines: COMM 1 and COMM 2. To maximize data transmission rates, UDP (User Datagram Protocol) was used in preference over TCP (Transmission Control Protocol). Because the telemetry transmission incurred almost 50%-375 loss on average over the flight, three black-box recorders were installed on the gondola to safely record all data.

The AESOP-Lite instrument and data recorders were recovered in good shape. Preliminary inspection indicated that the instrument operated at the expected efficiency.380 Analysis of flight data and further MC simulations are ongoing to determine the detector's efficiency and derive the flux of primary electrons and positrons. Upcoming plans include refurbishing the instrument and upgrading the entry telescope's electronics in preparation for future385 flights, to explore different solar modulation epochs.

5. Acknowledgments

We would like to thank Matthew Collins, Forest Martinez-Mckinney, and Yang Zhou for their help in the design, construction and integration of the instrument. We thank Chris Field and the CSBF for their support during the integration period in Palestine, Texas, and for the successful balloon flight. We thank Esrange for their support during the flight campaign. This work is supported by the NASA award 80NSSC19K0746.

References

References

- [1] M. Casolino, et al., Launch of the space experiment PAMELA, *Advances in Space Research* 42 (3) (2008) 455–466. doi: 10.1016/j.asr.2007.07.023. URL <http://www.sciencedirect.com/science/article/pii/S0273117707007831>
- [2] M. Aguilar, others, (AMS Collaboration), Electron and Positron Fluxes in Primary Cosmic Rays Measured with the Alpha Magnetic Spectrometer on the International Space Station, *Physical Review Letters* 113 (12). doi:10.1103/PhysRevLett.113.121102. URL <https://link.aps.org/doi/10.1103/PhysRevLett.113.121102>
- [3] O. Adriani, others CALET Collaboration, Energy Spectrum of Cosmic-Ray Electron and Positron from 10 GeV to 3 TeV Observed with the Calorimetric Electron Telescope on the International Space Station, *Physical Review Letters* 119 (18). doi:10.1103/PhysRevLett.119.181101. URL <https://link.aps.org/doi/10.1103/PhysRevLett.119.181101>
- [4] F. Gargano, DAMPE collaboration, The DAMPE experiment: 2 year in orbit, *Journal of Physics: Conference Series* 934 (2017) 012015. doi:10.1088/1742-6596/934/1/012015. URL <http://stacks.iop.org/1742-6596/934/i=1/a=012015?key=crossref.c7b72e42c6b48a5cdb06944fcb094a11>
- [5] E. S. Seo, et al., Cosmic Ray Energetics And Mass for the International Space Station (ISS-CREAM), *Advances in Space Research* 53 (10) (2014) 1451–1455. doi:10.1016/j.asr.2014.01.013. URL <http://www.sciencedirect.com/science/article/pii/S0273117714000313>
- [6] E. C. Stone, et al., Voyager 1 Observes Low-Energy Galactic Cosmic Rays in a Region Depleted of Heliospheric Ions, *Science* 341 (6142) (2013) 150–153. doi:10.1126/science.1236408. URL <http://science.sciencemag.org/content/341/6142/150>
- [7] D. Hovestadt, et al., A detector system for cosmic ray electrons, *Nuclear Instruments and Methods* 85 (1) (1970) 93–100. doi:10.1016/0029-554X(70)90125-4. URL <http://www.sciencedirect.com/science/article/pii/0029554X70901254>
- [8] J. M. Clem, et al., Solar Modulation of Cosmic Electrons, *The Astrophysical Journal* 464 (1996) 507. doi:10.1086/177340. URL <http://adsabs.harvard.edu/abs/1996ApJ...464..507C>
- [9] P. Evenson, et al., Cosmic Ray Electron Spectrum in 2009 (2009) 5.
- [10] O. Adriani, et al., An anomalous positron abundance in cosmic rays with energies 1.5–100 GeV, *Nature* 458 (2009) 607. URL <http://dx.doi.org/10.1038/nature07942>
- [11] T. F. L. Collaboration, M. Ackermann, et al., Measurement of separate cosmic-ray electron and positron spectra with the Fermi Large Area Telescope, *Physical Review Letters* 108 (1), arXiv: 1109.0521. doi:10.1103/PhysRevLett.108.011103. URL <http://arxiv.org/abs/1109.0521>

- [12] M. Tanabashi, et al., Review of particle physics, Phys. Rev. D 98 (2018) 030001. doi:10.1103/PhysRevD.98.030001.
URL <https://link.aps.org/doi/10.1103/PhysRevD.98.030001>
- [13] Design of permanent multipole magnets with oriented rare earth cobalt material 169 (1). doi:10.1016/0029-554X(80)90094-4.
URL <http://www.sciencedirect.com/science/article/pii/0029554X80900944>
- [14] W. Atwood, et al., Design and initial tests of the Tracker-converter of the Gamma-ray Large Area Space Telescope, Astroparticle Physics 28 (4-5) (2007) 422–434. doi:10.1016/j.astropartphys.2007.08.010.
URL <http://linkinghub.elsevier.com/retrieve/pii/S0927650507001302>
- [15] R. P. Johnson, et al., Tracker Readout ASIC for Proton Computed Tomography Data Acquisition, IEEE transactions on nuclear science 60 (5 Pt 1) (2013) 3262–3269. doi:10.1109/TNS.2013.2274663.
URL <https://www.ncbi.nlm.nih.gov/pmc/articles/PMC3957097/>
- [16] R. P. Johnson, et al., A Fast Experimental Scanner for Proton CT: Technical Performance and First Experience With Phantom Scans, IEEE Transactions on Nuclear Science 63 (1) (2016) 52–60. doi:10.1109/TNS.2015.2491918.
- [17] J. D. Sullivan, Geometrical factor and directional response of single and multi-element particle telescopes, Nuclear Instruments and Methods 95 (1971) 5. doi:10.1016/0029-554X(71)90033-4.
URL <http://adsabs.harvard.edu/abs/1971NucIM..95....5S>
- [18] R. Frühwirth, Application of kalman filtering to track and vertex fitting, Nuclear Instruments and Methods in Physics Research Section A: Accelerators, Spectrometers, Detectors and Associated Equipment 262 (2) (1987) 444 – 450. doi:https://doi.org/10.1016/0168-9002(87)90887-4.
URL <http://www.sciencedirect.com/science/article/pii/0168900287908874>
- [19] V. Khachatryan, et al., Measurement of the charge ratio of atmospheric muons with the CMS detector, Physics Letters B 692 (2) (2010) 83–104. doi:10.1016/j.physletb.2010.07.033.
URL <http://www.sciencedirect.com/science/article/pii/S0370269310008725>